

Need for Rationally Designed SnWO₄ Photo(electro)catalysts to Overcome the Performance Limitations for O₂ and H₂ Evolution Reactions

Luis Miguel Azofra, Luigi Cavallo, Jean-Marie Basset, and Moussab Harb*



Cite This: <https://doi.org/10.1021/acs.jpcc.0c11614>



Read Online

ACCESS |



Metrics & More

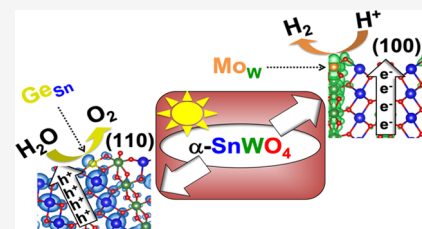


Article Recommendations



Supporting Information

ABSTRACT: Although the α -SnWO₄ material has recently been considered as a new good candidate for visible-light-driven photo(electro)chemical water splitting, the performance is still low and requires further improvement. Here, we present a deep fundamental work on the influence of the various possible facets exposed on this material for oxygen and hydrogen evolution reactions using hybrid density functional theory. The energetic, electronic, water redox, and charge carrier transport features of the four possible (100), (010), (001), and (110) facets (low-Miller index surfaces) are investigated, and significant anisotropic nature is revealed. The relevant properties of each facet to the water oxidation/reduction reactions are correlated with the surface W coordination number. Taking into account the stability and combining optoelectronic and water redox features together of each surface, our work demonstrates that the (110) facet is photocatalytically the best candidate for the OER, while the (100) facet is the best candidate for the HER. Their transport characteristics are found to be much better than those obtained for the three major (121), (210), and (111) facets of synthesized α -SnWO₄ samples. Substitutional Ge at the Sn site and Mo at the W site on the two (110) and (100) facets are expected to increase the rates of the water oxidation/reduction reactions. An analysis of the reaction mechanism for the OER in (110)-oriented α -SnWO₄ reveals a promising performance of this facet for electrocatalytic water oxidation. These outcomes will greatly motivate experimentalists for carefully designing (110)- and (100)-oriented α -SnWO₄ samples to enhance the photo(electro)catalytic OER and photocatalytic HER performances.



INTRODUCTION

Solar water splitting for hydrogen production by photo(electro)catalysis using a semiconductor-based heterogeneous catalyst is one of the promising technologies for a clean energy future and a sustainable green environment at low cost.^{1–6} Considerable efforts have been made on developing an operating and ideal photocatalyst by monitoring its fundamental characteristics to acquire both O₂ and H₂ evolution reactions, HER and OER, and to achieve high conversion efficiency. The photogenerated holes and electrons involved in water-splitting reactions are placed at the valence band maximum and conduction band minimum of the photocatalyst (VBM and CBM). Appropriate VBM and CBM energy positions should lie below O₂/H₂O and above H⁺/H₂ potentials, respectively, to drive the holes and electrons for oxidizing water and reducing protons.^{7,8} The well-delocalized involved orbitals in the VBM/CBM electronic states are vital to secure good hole/electron mobility throughout the material crystal lattice to the surface.^{9–13} To enhance the photocatalytic properties, various strategies have been outlined either by introducing co-catalysts on the electrode surfaces to improve the kinetics of holes and electron transfers to the electrolyte or by fabricating heterojunctions.^{14–17} Among them, exposed facet engineering has been reviewed as a promising way to tune

the material characteristics and improve the photocatalytic activity results.^{18–21}

Previously, several oxide- and (oxy)nitride-based photocatalysts have been shown as appropriate candidates for solar water splitting.^{6,22–27} α -SnWO₄ has recently been considered as a new good candidate due to its small band gap in the 1.6–2.1 eV range and an onset potential in the –0.14 to 0.05 V range vs RHE.^{28–34} Unfortunately, the different photoelectrodes prepared so far for α -SnWO₄ have given poor performance because of the low carrier transport to the surface.^{29,31,32} Therefore, there is a crucial need for a deep investigation of the optoelectronic and redox characteristics of α -SnWO₄ as they can strongly affect its photoelectrochemical performance. Various synthesis protocols of α -SnWO₄ samples led to various morphologies and then diverse photocatalytic results.^{28–34} To help for easier charge separation and higher efficiency, careful synthesis approaches for α -SnWO₄ with particular exposed facets are thus indispensable.

Received: December 30, 2020

Revised: April 5, 2021

A few theoretical studies appeared on the bulk features of α -SnWO₄^{28,31,35,36} whereas no work was done on the characteristics of its surfaces. A deep investigation of the various possible surfaces together with the relevant properties of each surface to photoredox reactions is required to identify the main factors limiting its performance and then the discrepancy in the photocatalytic features. In previous computational reports, we studied key bulk properties of various photocatalysts including α -SnWO₄^{9–13,29,37–42} by means of the density functional theory (DFT) with the hybrid Hyeed–Scuseria–Ernzerhof (HSE06) exchange–correlation functional.^{43,44} Their experimental band gap and relative band alignment to water-splitting limits were accurately reproduced, giving a good reliability of this method.^{9–13,29,37–42} Following this methodology, we recently identified the ideal facets for the OER and HER of the largely used TiO₂ and Ta₃N₅ photocatalysts.^{45,46} We also showed a strong influence of the major experimental exposed facets acquired for the common BiVO₄ photocatalyst on its water-splitting performance.⁴⁷

Here, we present the impact of the various possible exposed facets on the α -SnWO₄ photo(electro)catalyst performance for water-splitting reactions in the framework of a deep fundamental work based on the DFT–HSE06 computational methodology. We carried out calculations for the energetic, electronic, water redox, and charge carrier transport features of the four possible (100), (010), and (001), and (110) facets (low-Miller index surfaces). Then, we predicted the best facet candidates for the OER and HER by taking into account the stability and combining water redox, electronic structure, and charge carrier transport features of each surface. Moreover, we partially modified the best facets by replacing the active sites with the nearest-neighbor isoelectronic elements. A great enhancement in the orbital hybridization characters of the VBM/CBM electronic states with the corresponding OER/HER active sites was revealed. In addition, we compared the results of the best facets with those obtained for the three major (121), (210), and (111) ones of synthesized samples, and relevant information was found. Finally, for those most promising facets, supporting calculations on the mechanism for the electrochemical water oxidation and proton reduction reactions were also shown, with a particular interest in the effect of dopants on the electrocatalytic performances. As a consequence, these findings will encourage experimentalists to adopt a careful design of active α -SnWO₄ samples with particular exposed facets for enhancing the photo(electro)-catalytic water-splitting performance toward the OER and HER.

METHODOLOGY

The four possible (100), (010), and (001), and (110) low-Miller index α -SnWO₄ exposed facets as well as the three predominated (121), (210), and (111) facets obtained experimentally for this material were constructed based on the commonly bulk orthorhombic crystal lattice shown in Figure 1.^{28–32} The unit cell model consisting of four functional units, Sn₄W₄O₁₆ or 24 atoms, was taken here as the starting material for generating the different surfaces. Accordingly, the slab models were acquired by cleaving the bulk along the corresponding Miller (*hkl*) crystallographic plane. Each slab has several layers chosen adequately for surface modeling in which the center region exhibits the corresponding bulklike structure. Various possible surface terminations were explored for each slab to find the most stable one by maintaining the

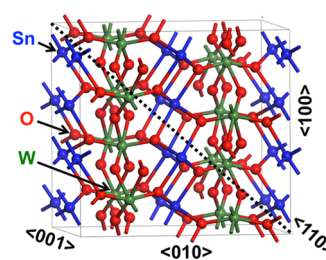


Figure 1. Crystal structure depiction of bulk α -SnWO₄ on the basis of the 2×2 supercell together with the four possible $\langle 110 \rangle$, $\langle 100 \rangle$, $\langle 010 \rangle$, and $\langle 001 \rangle$ crystallographic orientations. O is in red, W in green, and Sn in blue.

stoichiometry and by keeping the equivalent top and bottom layer sides. Constructed symmetric slabs were possible for all of the explored facets except for (010), where an asymmetric slab was the only way to keep the stoichiometry due to the particular atomic repartition along this crystallographic orientation, revealing WO₆ layers stacked in the *ac* plane and connected between each other with Sn species. The vacuum width for all slabs was set at 15 Å to avoid periodic interactions between the top and bottom sides of the surface. Benchmark tests were performed with different thicknesses to ensure the optimum required thickness and sufficient convergence of electronic properties of each slab, similarly as recently reported for TiO₂, Ta₃N₅, and BiVO₄ surfaces.^{45–47} For the (110) slab model, six layers or 72 atoms were needed with a thickness of 15 Å. Five atomic layers or 60 atoms were required for describing the (100) slab model with a thickness of 12 Å. For the (010) slab model, five layers or 60 atoms were needed with a thickness of 27 Å. Seven layers expended on a thickness of 17 Å with 84 atoms were necessary for describing the (001) slab model. For the (121) slab model, seven atomic layers or 96 atoms were required with a thickness of 12 Å. Seven layers or 96 atoms were needed with 10 Å thickness for describing the (210) slab model. For the (111) slab model, seven atomic layers expended on a thickness of 14 Å with 96 atoms were necessary.

The valence and conduction band edge energy positions of the material were calculated by aligning the electronic structure to a reference scale of energy.^{48–52} Starting from the electronic structure calculation of the optimized slab, the absolute energy of the band edges was obtained. Then, the vacuum energy was computed from the local potential profile in the vacuum direction. Then, the difference between the band energies of the slab and the vacuum energy led to the band positions relative to vacuum. More details about this protocol are reported in refs 11, 12, 37, 45–47.

The hole and electron transport features were judged from the electronic population analysis and visualized by the partial charge density maps at the band edges. Delocalized and hybridized orbitals over the crystal lattice of the material going from bulk to the surface can guarantee a smooth charge carrier migration to the surface reaching the co-catalysts. More details about this protocol are given in refs 9–13, 42.

Finally, the mechanisms for the electrochemical water oxidation, i.e., $2\text{H}_2\text{O} \rightleftharpoons \text{O}_2 + 4\text{H}^+ + 4\text{e}^-$, and proton reduction, i.e., $\text{H}^+ + \text{e}^- \rightleftharpoons 1/2\text{H}_2$, were studied in the framework of the proton-coupled electron transfer (PCET) approach.⁵³ In this sense, the oxygen evolution reaction (OER) was modeled following the reaction mechanism steps: (i) $* + \text{H}_2\text{O} \rightleftharpoons *\text{OH} + \text{H}^+ + \text{e}^-$; (ii) $*\text{OH} \rightleftharpoons *\text{O} + \text{H}^+ + \text{e}^-$;

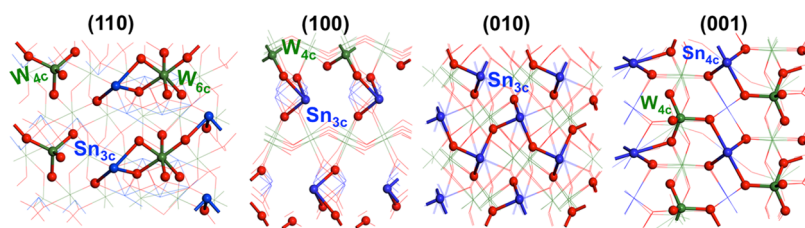


Figure 2. Lowest-energy structures (top views) of the (110), (100), (010), and (001) α -SnWO₄ facets. O is in red, W in green, and Sn in blue. The coordination numbers are indicated for the elements on each facet.

(iii) $*\text{O} + \text{H}_2\text{O} \rightleftharpoons *\text{OOH} + \text{H}^+ + \text{e}^-$; (iv) $*\text{OOH} \rightleftharpoons * + \text{O}_2 + \text{H}^+ + \text{e}^-$, where “*” denotes the chemical surface.

COMPUTATIONAL DETAILS

DFT calculations with periodic boundary conditions were carried out using the Vienna Ab initio Simulation Package (VASP)^{54–57} with the Perdew–Burke–Ernzerhof (PBE) exchange–correlation potential.⁵⁸ The core electrons were sketched by projector-augmented wave (PAW) potentials,⁵⁹ with $5s^25p^2$, $5d^46s^2$, $2s^22p^4$, $4s^24p^2$, and $4d^45s^2$ valence electrons treated explicitly in the plane wave descriptions for Sn, W, O, Ge, and Mo, respectively. A kinetic cutoff energy of 400 eV was consistently used in our calculations for electron wave function expansion. The atomic positions were fully relaxed with the conjugate gradient procedure until the residual forces vanished within 0.01 eV/Å and the electronic convergence for each supercell was below 10^{-6} eV. Upon several tests evaluating the accuracy of the calculations, the Monkhorst–Pack k -point mesh⁶⁰ for sampling the Brillion zone was set at $3 \times 5 \times 1$ for (110), $5 \times 3 \times 1$ for (100), $5 \times 5 \times 1$ for (010), $3 \times 5 \times 1$ for (001), $5 \times 3 \times 1$ for (121), $1 \times 7 \times 1$ for (210), and $3 \times 5 \times 1$ for (111) slabs.

Based on the optimized geometries obtained with the PBE functional, the electronic structure calculations were conducted at the level of the more expensive screened Coulomb hybrid Heyd–Scuseria–Ernzerhof (HSE06)^{43,44} functional using VASP. This method has been proven to provide higher band-gap accuracy of semiconductors compared to the standard GGA functional.^{9–13,29,37–42} The electronic property analysis covered the density of states (DOS) along with the orbital density maps for the band edges in terms of each element contribution.

By means of the local potential profile going from the bulk to a region away from the surface computed using the HSE06 functional, the vacuum energy was acquired. The dipole corrections perpendicularly to the surface were applied to alleviate errors in the periodic boundary conditions.⁶¹ More detailed information about this procedure has been previously reported in refs 11, 12, 37, 45–47.

All energy calculations for the study of the reaction mechanisms for the OER and HER were performed using the PBE functional. Vibrational frequencies were calculated over the Γ point to obtain zero-point energies (ZPEs), thermal corrections, and entropy contributions. At this step, explicit dispersion correction terms to the free energy were also employed through the use of the D3 method with the standard parameters programmed by Grimme and co-workers.^{62,63} In this sense, once optimized the clean surfaces, all intermediate states were optimized by applying structural constraints to the inner layers. Specifically, only the atoms of the last two (most exposed) surfaces were set free, while the rest of the atoms were frozen during optimization and frequency calculations.

RESULTS AND DISCUSSION

Structural, Energetic, Electronic, and Water Redox Characteristics of the (100), (010), (001), and (110) α -SnWO₄ Surface Planes. Bulk α -SnWO₄ possesses an orthorhombic crystal structure (space group $Pnna$) composed of 2D sheets of distorted corner-sharing WO₆ octahedra and separated by layers of 4-fold coordinated edge-sharing Sn²⁺ ions through O (Figure 1). Our PBE-based optimized lattice parameters ($a = 5.59$ Å, $b = 11.63$ Å, $c = 4.98$ Å, and $\alpha = \beta = \gamma = 90^\circ$) were found in excellent agreement with the experimental values ($a = 5.62$ Å, $b = 11.74$ Å, $c = 4.98$ Å, and $\alpha = \beta = \gamma = 90^\circ$).^{28,29,31,32,35} Inside the crystal lattice of the bulk material, four possible $\langle 100 \rangle$, $\langle 010 \rangle$, $\langle 001 \rangle$, and $\langle 110 \rangle$ crystallographic directions exist; thus, four possible (100), (010), (001), and (110) facets (low-Miller index surfaces) are present on top of this crystalline material (Figure 2). The (110) facet reveals three-coordinated Sn with four- and six-coordinated W, while the (100) facet reveals three-coordinated Sn with only four-coordinated W. For the (010) facet, the top layer is only made of three-coordinated Sn with W species presented in sublayers, whereas the (001) facet reveals four-coordinated Sn with four-coordinated W. The calculated surface energies for the four (110), (100), (010), and (001) facets were 0.57, 0.31, 0.85, and 1.06 J/m², respectively. Note that the (010) surface energy is 0.3–0.5 J/m² higher than that obtained for (110) and (100). The (001) surface energy is 0.5–0.7 J/m² higher than that obtained for (110) and (100). This makes the two (110) and (100) facets thermodynamically more stable than the (010) and (001). The less stability of the two (010) and (001) facets come from the absence of W at the top layer of the (010) facet and the presence of four-coordinated Sn on the top layer of the (001) facet. Despite the lower stability of (010) and (001) facets compared to that obtained for (110) and (100), we considered them for further discussion and deeper analysis as they might be stabilized by specific controllable preparation methods.

For the bulk counterpart, our predicted band gap (1.5 eV) was found to be in good agreement with the reported measured ones (from 1.6 to 1.9 eV).^{28–34} Our HSE06-based computed value revealed much higher accuracy compared to the PBE-based one (0.8 eV).^{28–34} The CBM states are made by empty W 5d orbitals. The VBM states are made by occupied O 2p and Sn 5s orbitals, in line with the X-ray absorption spectroscopy results.³⁵ The hybridization character between O 2p and Sn 5s orbitals at the VBM is originated from the SnO₄ tetrahedra distortion, in accordance with the X-ray absorption spectroscopy data.³⁵ Similar contributions of orbitals at the CBM/VBM electronic states are also found in (110), (100), (010), and (001) α -SnWO₄ slabs. If we compare with the bulk material, the band gaps are 0.2–0.6 eV larger or 0.4 eV smaller. The (110) slab gives 1.8 eV, while the (100)

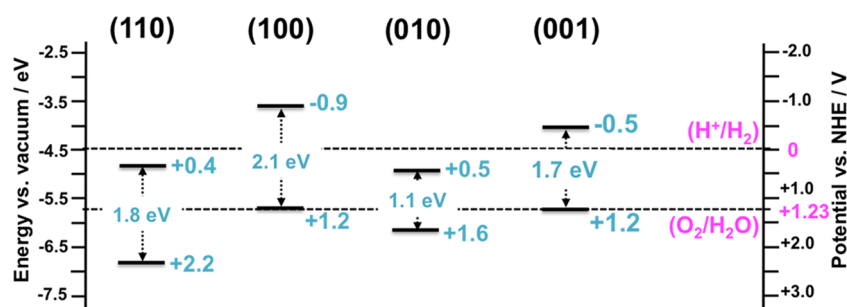


Figure 3. Band energy levels of the (110)-, (100)-, (010)-, and (001)-oriented α -SnWO₄ slabs vs vacuum.

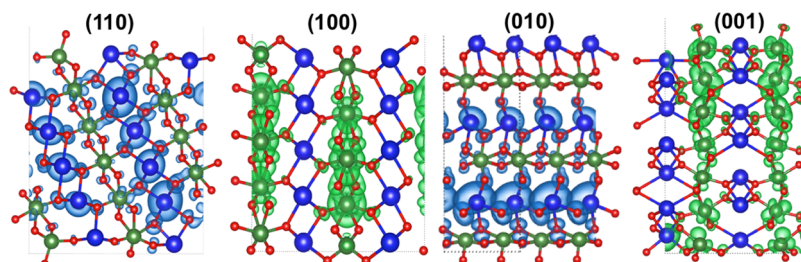


Figure 4. Orbital density maps for VBM (shown in blue) of (110) and (010) α -SnWO₄ slabs and for CBM (in green) of (100) and (001) α -SnWO₄ slabs.

slab gives 2.1 eV. For (010) and (001) slabs, band-gap values of 1.1 and 1.7 eV were obtained (Figure 3). Note that the average band gap for the four explored facets reveals better agreement with the experimental value than the bulk obtained one. These results highlight a significant impact of the exposed facets on the band gap of synthesized α -SnWO₄ samples.

The energy levels of the (110), (100), (010), and (001) α -SnWO₄ slabs were then defined with respect to vacuum. The VBM energies for the two (110) and (010) slabs are 1.0 and 0.4 eV below the O₂/H₂O level and the CBM energies are 0.4 and 0.5 eV below the H⁺/H₂ level, respectively (Figure 3). Since their CBM level is not correctly placed vs the H⁺/H₂ level, the excited electrons will not be able to reduce protons. Therefore, these facets are suitable for the OER only. The CBM energies for the (100) and (001) slabs are 0.9 and 0.5 eV higher than the H⁺/H₂ level, respectively, while their VBM energy is placed at the O₂/H₂O level (see Figure 3). Due to their wrong VBM level with respect to the O₂/H₂O level, the generated holes will not be able to oxidize water. Consequently, these two facets are only suitable for the HER. A similar trend in the redox properties between (100) and (001) can be recognized by the presence of four-coordinated W at the two facets. The radical downward shift in the band energies of (110) compared to those acquired for (100) and (001) originates from the presence of six-coordinated W at this facet (Figure 3). The strong modification in the redox signature of (010) with respect to (110), (100), and (001) can be understood by the appearance of only three-coordinated Sn without W species present in sublayers (Figure 3). These results highlight a strong anisotropic nature for the redox characteristics of the α -SnWO₄ photocatalyst as a function of the exposed facet.

Charge Carrier Transport Features toward the (100), (010), (001), and (110) α -SnWO₄ Surface Planes. We display in Figure 4 the partial charge density maps for VBM states of (110) and (010) α -SnWO₄ slabs as well as for CBM states of (100) and (001) α -SnWO₄ slabs. For the (100) and

(001) slabs, the density maps for the CBM states are well delocalized on all W 5d orbitals located in the lattice (see Figure 4). The W 5d orbital distribution over all W species is clear in both cases. These results lead to a smooth electron migration from bulk to (100) and (001) surfaces. With respect to the (110) slab, the partial density of the VBM state is well distributed over Sn 5s and O 2p orbitals, giving such hole mobility to the (110) surface (see Figure 4). Contrarily, the density for the VBM state of the (010) facet is localized strongly on the Sn 5s orbitals situated in the bulk (Figure 4). The density for the VBM state of (110) exhibits much more delocalization over all Sn toward the three-coordinated surface Sn (Figure 4). These results strongly limit the hole migration to the (010) facet and predict much better mobility of holes to the (110) facet against the (010) one. The similarities in the electron transport to (100) and (001) facets could be understood by the similar W species arrangement in the (100)- and (001)-oriented slab geometries (Figure 4). The drastic change in the hole transport to the (110) and (010) facets could also be explained by the appearance of Sn species over atomic planes almost perpendicular to the (110) facet and parallel to the (010) facet (Figure 4). These results also highlight a strong anisotropic nature for the optoelectronic characteristics of the α -SnWO₄ photocatalyst as a function of the exposed facet identity.

The two OER/HER co-catalysts must be placed on the best surface candidates to help for the hole/electron transfer kinetics to water. Taking into account the stability and combining optoelectronic and water redox features together of each facet, our work demonstrates that the (110) facet is photocatalytically the best candidate for the OER, while the (100) facet is the best candidate for the HER. The (010) facet is an inappropriate candidate neither for the HER nor for the OER. Based on that, the co-catalyst for the OER needs to be selectively anchored on the (110) facet of α -SnWO₄ and the co-catalyst for the HER on the (100) facet.

Here, the predicted results could provide the fundamental origin behind the poor photoelectrochemical water-splitting performance of this material.^{29,31,32} Overcoming this limitation requests a selective deposition of the co-catalyst for the HER on the (100) facet and that for the OER on the (110) facet. The four-coordinated W present on the (100) facet is the active site for the HER. The three-coordinated Sn present on the (110) facet would be the active site for the OER. Although the strong anisotropic nature of redox and carrier transport features of the various possible surfaces makes water splitting more complex, the presented concept will greatly guide the experimentalists for the choice of the most suitable deposition of the two HER and OER co-catalysts.

Ge-Doped (110) and Mo-Doped (100) α -SnWO₄ Surfaces for Enhanced Charge Carrier Accumulation. To enhance further the orbital hybridization characteristics of the VBM/CBM electronic states for the (110)/(100) α -SnWO₄ facets with the corresponding OER/HER active sites, we partially modified the two facets by replacing the active sites with the nearest-neighbor isoelectronic elements having a similar atomic radius to not perturb their chemical environment by the formation of such vacancies. The three-coordinated Sn present on the (110) facet was substituted by Ge and the four-coordinated W on the (100) facet by Mo. These two surface models led to the following stoichiometry: α -Sn_(1-x)Ge_xWO₄ with $x = 0.083$ for (110) and α -SnW_(1-y)Mo_yO₄ with $y = 0.1$ for (100). After structural optimization, Ge and Mo species maintained the same coordination numbers as obtained for Sn and W in the unmodified surfaces (Figure 5). The energy costs for substituting surface Sn by Ge on the (110) facet and surface W by Mo on the (100) facet were investigated using these expressions

$$E_{\text{form}}(110) = E[\alpha - \text{Sn}_{(1-x)}\text{Ge}_x\text{WO}_4] - E[\alpha - \text{SnWO}_4] + x \cdot E[\text{Sn}] - x \cdot E[\text{Ge}] \quad (1)$$

$$E_{\text{form}}(100) = E[\alpha - \text{SnW}_{(1-y)}\text{Mo}_y\text{O}_4] - E[\alpha - \text{SnWO}_4] + y \cdot E[\text{W}] - y \cdot E[\text{Mo}] \quad (2)$$

They include the electronic energies of (110) α -SnWO₄, (110) α -Sn_(1-x)Ge_xWO₄, (100) α -SnWO₄, and (100) α -SnW_(1-y)Mo_yO₄ slabs as well as the electronic energies of pure Sn, Ge, W, and Mo solids in their most stable crystal phases. Very slightly positive values of +0.02 and +0.08 eV were found for the reactions associated with expressions eqs 1 and 2, respectively. As the energy cost values are almost negligible, this confirms thermodynamically the possible modification of the two (110) and (100) facets by Ge and Mo, respectively. A minimal impact of substitutional Ge at the Sn site and Mo at the W site on the redox characteristics of (110) and (100) α -SnWO₄ facets was found (Figures 3 and 5). A relatively small downward shift in the VBM/CBM levels of (110) by 0.2 eV and a small downward shift in the CBM level of (100) by 0.1 eV were obtained. However, a positive effect of the presence of Ge and Mo on the charge carrier transport toward the (110) and (100) α -SnWO₄ surfaces was found (Figures 4 and 5). A great enhancement in the orbital hybridization characters of the VBM/CBM electronic states with the corresponding Ge 4s/Mo 4d for OER/HER active sites was obtained. This is expected to increase the amount of photogenerated holes/electrons on top of (110)/(100)

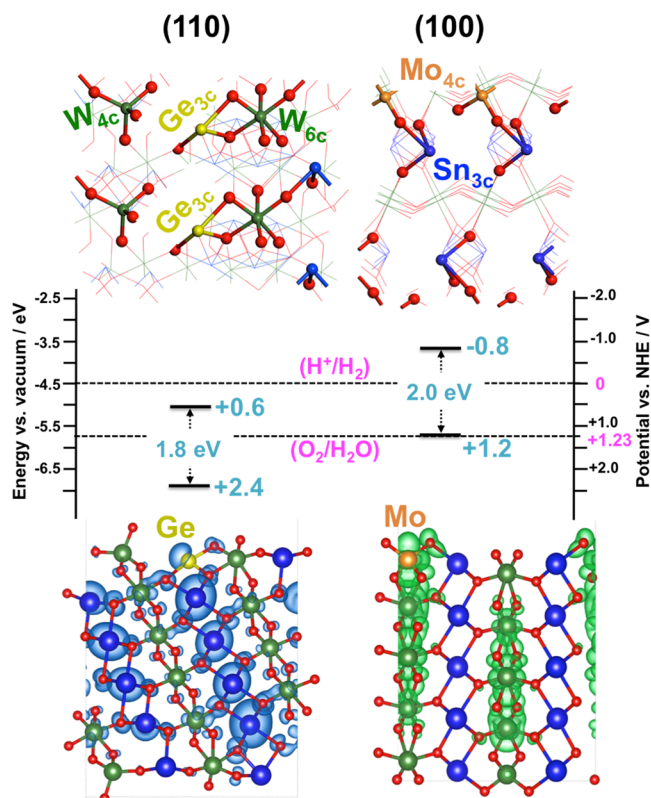


Figure 5. Atomic structures (top views), band levels vs NHE, and orbital density maps for the VBM state (in blue) and for the CBM state (in green) of (110) α -Sn_(1-x)Ge_xWO₄ ($x = 0.083$) and (100) α -SnW_(1-y)Mo_yO₄ ($y = 0.1$) surfaces. O is in red, Sn in blue, W in green, Ge in yellow, and Mo in orange.

surfaces and, therefore, the rates of the water oxidation/reduction reactions. The fundamental results obtained for the two (110) and (100) facets will encourage the experimentalists to synthesize and utilize these surfaces for the OER and HER.

Comparison with the Main Facets of Synthesized α -SnWO₄ Samples. Very recently,⁶⁴ we examined the fundamental characteristics of the five main (210), (121), (040), (200), and (111) facets obtained in synthesized α -SnWO₄ samples.^{28–34} The two experimental (040) and (200) facets are identical to the (010) and (100) ones. The two (210) and (121) facets are made of three-coordinated Sn with four- and five-coordinated W, respectively. They are different from the case of (110), where four- and six-coordinated W is present on top of the surface. The (111) facet is composed of three-coordinated Sn and four-coordinated W similarly as acquired in the (100) and (001) cases. The calculated surface energies of (121), (210), and (111) facets are 0.51, 0.48, and 0.55 J/m², respectively. As these values are very similar to those obtained for (110) and (100), those facets are competitive between each other in terms of chemical stability. Details on the DFT-based most stable surface atomic structures, band alignments, and charge density maps of the (121), (210), and (111) α -SnWO₄ are given in Figures S1–S3 in the Supporting Information.

Interestingly, the similar behavior in the W exposed species coordination number between the (111), (100), and (001) facets as well as in the exposed W coordination number between (121) and (210) facets led to a similarity in the electronic and redox characteristics. Moreover, the difference

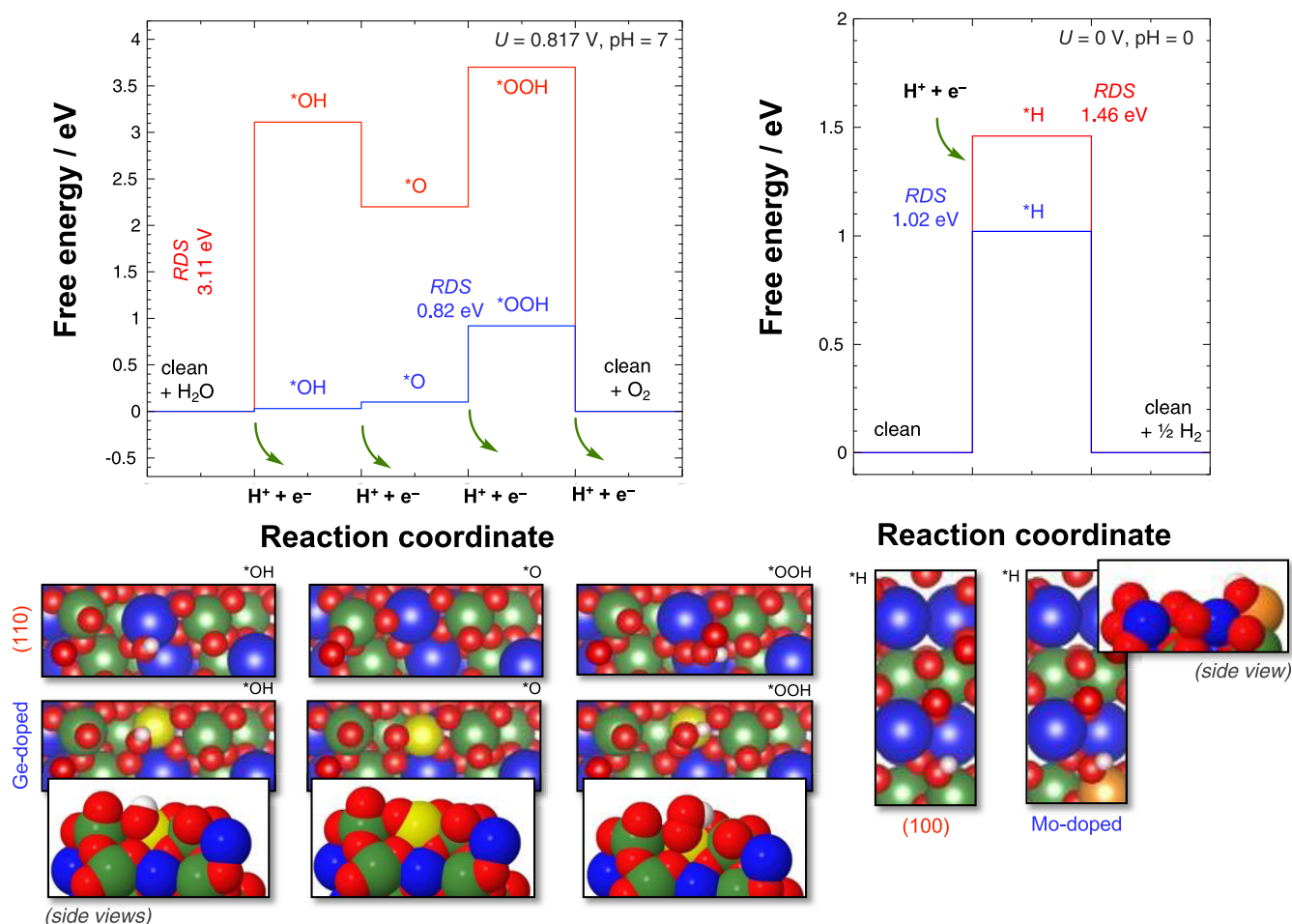


Figure 6. Free energy profiles for OER (left) and HER (right) mechanisms, catalyzed by (110) and (100) facets of α -SnWO₄, respectively. The doping of Ge in (110) and Mo in (100) facets was also examined. For the OER, pH = 7 and applied potential of $U = 0.817$ V were considered. For the HER, pH = 0 and $U = 0$ V. H is in white, O in red, Sn in blue, W in green, Ge in yellow, and Mo in orange.

in the exposed W coordination number on the (110) facet compared to (121) or (210) facets led to different electronic and redox characteristics. The (111) facet is predicted in terms of correct CBM position vs H^+/H_2 potential to be a suitable candidate only for the HER as acquired for (110) and (001). However, the (121) and (210) facets are predicted in terms of correct CBM and VBM positions vs H^+/H_2 and O_2/H_2O potentials to be appropriate candidates for the OER and HER, differently from the case of (110).

Although the redox features of (111), (100), and (001) facets as well as of (121) and (210) are similar, their charge carrier transport features are different because of the discrepancy in the Sn and W structural arrangements throughout the bulk toward these surfaces. Compared to those for (100) and (001) facets, the densities for the CBM states of the (121), (210), and (111) slabs clearly exhibit much less pronounced delocalization of W 5d orbitals throughout the lattice to the four- and five-coordinated surface W. These results predict an easier electron migration to (100) and (001) surfaces rather than to (121), (210), or (111) ones. Compared to that for the (110) facet, the partial charge densities for VBM states of the (121) and (210) slabs clearly reveal much less pronounced Sn 5s orbital delocalization throughout the lattice toward the three-coordinated surface Sn. These results predict an easier hole migration to the (110) facet against (121) or (210) ones. Note that the highest surface energy found for the

(1001) facet compared to all other facets indicates the least stability of this surface and explains the reason why (001) was not reported experimentally. However, such a kinetic effect present in controllable preparation methods might stabilize this surface. The interesting fundamental results obtained for the (001) facet will certainly motivate the experimentalists to target, stabilize, and test it for the HER.

Electrocatalytic Performances of Ge-Doped (110) and Mo-Doped (100) for the OER and HER. Having into consideration the good performances of (110) and (100) facets for the photocatalytically promoted OER and HER, we also examined their surface chemistry and their role in the electrocatalytic water oxidation and proton reduction mechanisms. Thus, the (110) facet is characterized by the exposure of Sn species, being the only active sites capable of retaining the intermediate species during the OER process. Electrochemical water oxidation, consisting of the four successive elementary reactions detailed in Figure 6 (left, red profile), seems to be highly inefficient given the very high overpotential that this material demands. Specifically, the first oxidation elementary step, $* + H_2O \rightleftharpoons *OH + H^+ + e^-$, exhibits a thermodynamic impediment of 3.11 eV at neutral pH and an applied potential of 0.817 V vs SHE. This, representing the rate-determining step (RDS) of the whole electrochemical process, indicates the low O-philicity that surface Sn exhibits. These results heavily contrast with the ones observed for the Ge-doped (110) facet,

whose free energy profile is displayed in blue in Figure 6 (left). At the same conditions of pH = 7 and applied $U = 0.817$ V, both oxidation of H_2O into $^*\text{OH}$ and oxidation of $^*\text{OH}$ into $^*\text{O}$ are slightly nonspontaneous reactions. The third elementary oxidation step, comprising $^*\text{O} + \text{H}_2\text{O} \rightleftharpoons ^*\text{OOH} + \text{H}^+ + \text{e}^-$, represents the rate-determining step for the Ge-doped case with an OER overpotential of 0.82 V. This simple substitution of Sn by Ge turns this material into a promising OER catalyst, decreasing the RDS in 2.29 eV. For the case of the HER (Figure 6, right), the substitution of W by Mo in (100) surface entails a decrease from 1.46 eV (red) to 1.02 eV (blue) for the $\text{H}^+ + \text{e}^- \rightleftharpoons ^*\text{H}$ elementary reaction. This reveals a greater stability of the $-\text{MoOH}$ moiety with respect to the $-\text{WOH}$ in the nondoped surface, specifically 0.44 eV for pH = 0 and when there is no applied potential ($U = 0$ V). Despite this improvement, the production of H_2 via proton reduction seems to be somehow an energy-expensive process. Undoubtedly, the good performance of the OER in the Ge-doped (110) surface should get all of the attention from the experimental community for the development of efficient OER electrocatalysts.

CONCLUSIONS

We have presented a deep fundamental work on the impact of the various possible facets exposed on the $\alpha\text{-SnWO}_4$ photo(electro)catalyst material for oxygen and hydrogen evolution reactions using hybrid density functional theory. The energetic, electronic, water redox, and charge carrier transport features of the four possible (100), (010), (001), and (110) facets (low-Miller index surfaces) were investigated, and significant anisotropic nature was revealed. The relevant properties of each facet to the water oxidation/reduction reactions were linked to the coordination number of surface W.

By taking into account the stability and combining water redox and optoelectronic features of each facet, our work demonstrated that the (110) facet is photocatalytically the best candidate for the OER and (100) facet for the HER. Their charge carrier transport characteristics were found to be much better than those obtained for the three major (121), (210), and (111) facets of synthesized $\alpha\text{-SnWO}_4$ samples.

Substitutional Ge at the Sn site and Mo at the W site on the two (110) and (100) facets revealed a great enhancement in the orbital hybridization characters of the VBM/CBM electronic states with the corresponding Ge 4s/Mo 4d for OER/HER active sites. This is expected to amplify the amount of generated holes/electrons on top of (110)/(100) facets. Therefore, the rates of the water oxidation and reduction reactions are expected to be greatly enhanced.

The results obtained from this work could give the fundamental explanations behind the poor photoelectrochemical water-splitting performance of this material. A rational way was proposed to overcome this limitation based on depositing the OER co-catalyst on the (110) facet and the HER co-catalyst on the (100) facet.

The analysis of the surface chemistry in (110)- and (100)-oriented $\alpha\text{-SnWO}_4$ samples and the doping of these surfaces with Ge and Mo atoms, in each case, revealed a promising performance of the Ge-doped (110) surface as an electrocatalyst for the OER, calculating a theoretical overpotential of just 0.82 V vs $\text{H}_2\text{O}/\text{O}_2$.

The useful concept described here will efficiently motivate/ guide experimentalists toward enhancing the photo(electro)-chemical OER and photochemical HER performances by

following a careful design of (110)- and (100)-oriented $\alpha\text{-SnWO}_4$ samples.

ASSOCIATED CONTENT

Supporting Information

The Supporting Information is available free of charge at <https://pubs.acs.org/doi/10.1021/acs.jpcc.0c11614>.

Cartesian coordinates for the optimized structures corresponding to the most relevant predicted surfaces for the OER and HER. DFT-based most stable surface atomic structures, band alignments, and charge density maps of the (121), (210), and (111) $\alpha\text{-SnWO}_4$ facets (PDF)

AUTHOR INFORMATION

Corresponding Author

Moussab Harb – KAUST Catalysis Center, Physical Sciences and Engineering Division, King Abdullah University of Science and Technology (KAUST), Thuwal 23955-6900, Saudi Arabia; orcid.org/0000-0001-5540-9792; Phone: +966-012-8080788; Email: moussab.harb@kaust.edu.sa

Authors

Luis Miguel Azofra – Instituto de Estudios Ambientales y Recursos Naturales (i-UNAT), Universidad de Las Palmas de Gran Canaria (ULPGC), 35017 Las Palmas de Gran Canaria, Spain; orcid.org/0000-0003-4974-1670

Luigi Cavallo – KAUST Catalysis Center, Physical Sciences and Engineering Division, King Abdullah University of Science and Technology (KAUST), Thuwal 23955-6900, Saudi Arabia; orcid.org/0000-0002-1398-338X

Jean-Marie Basset – KAUST Catalysis Center, Physical Sciences and Engineering Division, King Abdullah University of Science and Technology (KAUST), Thuwal 23955-6900, Saudi Arabia; orcid.org/0000-0003-3166-8882

Complete contact information is available at: <https://pubs.acs.org/10.1021/acs.jpcc.0c11614>

Notes

The authors declare no competing financial interest.

ACKNOWLEDGMENTS

This research was supported by the King Abdullah University of Science and Technology (KAUST). We are also grateful to the KAUST Supercomputing Laboratory using the super-computer Shaheen II for providing the computational resources.

REFERENCES

- (1) van de Krol, R.; Parkinson, B. A. Perspectives on the Photoelectrochemical Storage of Solar Energy. *MRS Energy Sustainability* **2017**, *4*, No. 13.
- (2) Anantharaj, S.; Ede, S. R.; Sakthikumar, K.; Karthick, K.; Mishra, S.; Kundu, S. Recent Trends and Perspectives in Electrochemical Water Splitting with an Emphasis on Sulfide, Selenide, and Phosphide Catalysts of Fe, Co, and Ni: A Review. *ACS Catal.* **2016**, *6*, 8069–8097.
- (3) Maeda, K.; Domen, K. Photocatalytic Water Splitting: Recent Progress and Future Challenges. *J. Phys. Chem. Lett.* **2010**, *1*, 2655–2661.
- (4) Kudo, A.; Miseki, Y. Heterogeneous Photocatalytic Materials for Water Splitting. *Chem. Soc. Rev.* **2009**, *38*, 253–278.

- (5) Inoue, Y. Photocatalytic Water Splitting by RuO₂-Loaded Metal Oxides and Nitrides with d⁰- and d¹⁰-Related Electronic Configurations. *Energy Environ. Sci.* **2009**, *2*, 364–386.
- (6) Maeda, K.; Domen, K. New Non-Oxide Photocatalysts Designed for Overall Water Splitting Under Visible Light. *J. Phys. Chem. C* **2007**, *111*, 7851–7861.
- (7) Malathi, A.; Madhavan, J.; Ashokkumar, M.; Arunachalam, P. A Review on BiVO₄ Photocatalyst: Activity Enhancement Methods for Solar Photocatalytic Applications. *Appl. Catal., A* **2018**, *555*, 47–74.
- (8) Linsebigler, A. L.; Lu, G.; Yates, J. T. Photocatalysis on TiO₂ Surfaces: Principles, Mechanisms, and Selected Results. *Chem. Rev.* **1995**, *95*, 735–758.
- (9) Harb, M.; Sautet, P.; Raybaud, P. Origin of the Enhanced Visible-Light Absorption in N-Doped Bulk Anatase TiO₂ from First-Principles Calculations. *J. Phys. Chem. C* **2011**, *115*, 19394–19404.
- (10) Harb, M.; Masih, D.; Ould-Chikh, S.; Sautet, P.; Basset, J.-M.; Takanabe, K. Determination of the Electronic Structure and UV-Vis Absorption Properties of (Na_{2-x}Cu_x)Ta₄O₁₁ from First-Principle Calculations. *J. Phys. Chem. C* **2013**, *117*, 17477–17484.
- (11) Harb, M.; Cavallo, L.; Basset, J.-M. Major Difference in Visible-Light Photocatalytic Features Between Perfect and Self-Defective Ta₃N₅ Materials: A Screened Coulomb Hybrid DFT Investigation. *J. Phys. Chem. C* **2014**, *118*, 20784–20790.
- (12) Harb, M.; Cavallo, L. Toward the Design of New Suitable Materials for Solar Water Splitting Using Density Functional Theory. *ACS Omega* **2018**, *3*, 18117–18123.
- (13) Irani, R.; Ahmet, I. Y.; Jang, J.-W.; Berglund, P.; Plate, P.; Hohn, C.; Bottger, R.; Schmitt, S. W.; Dubourdieu, C.; Lardhi, S.; et al. Nature of Nitrogen Incorporation in BiVO₄ Photoanodes through Chemical and Physical Methods. *Sol. RRL* **2019**, *4*, No. 1900290.
- (14) Lin, F.; Wang, D.; Jiang, Z.; Ma, Y.; Li, J.; Li, R.; Li, C. Photocatalytic Oxidation of Thiophene on BiVO₄ with Dual Co-Catalysts Pt and RuO₂ Under Visible Light Irradiation Using Molecular Oxygen as Oxidant. *Science* **2012**, *5*, 6400–6406.
- (15) Cao, T.; Li, Y.; Wang, C.; Zhang, Z.; Zhang, M.; Shao, C.; Liu, Y. Bi₄Ti₃O₁₂ Nanosheets/TiO₂ Submicron Fibers Heterostructures: in Situ Fabrication and High Visible Light Photocatalytic Activity. *J. Mater. Chem.* **2011**, *21*, 6922–6927.
- (16) Grigioni, I.; Stamplecoskie, K. G.; Selli, E.; Kamat, P. V. Dynamics of Photogenerated Charge Carriers in WO₃/BiVO₄ Heterojunction Photoanodes. *J. Phys. Chem. C* **2015**, *119*, 20792–20800.
- (17) Yao, S.; Zhang, M.; Di, J.; Wang, Z.; Long, Y.; Li, W. Preparation of α -SnWO₄/SnO₂ Heterostructure with Enhanced Visible-Light-Driven Photocatalytic Activity. *Appl. Surf. Sci.* **2015**, *357*, 1528–1535.
- (18) Bai, L.; Jiang, W.; Gao, C.; Zhong, S.; Zhao, L.; Li, Z.; Bai, S. Facet Engineered Interface Design of NaYF₄:Yb,Tm Upconversion Nanocrystals on BiOCl Nanoplates for Enhanced Near-Infrared Photocatalysis. *Nanoscale* **2016**, *8*, 19014–19024.
- (19) Martin, D. J.; Umezawa, N.; Chen, X.; Ye, J.; Tang, J. Facet Engineered Ag₃PO₄ for Efficient Water Photooxidation. *Energy Environ. Sci.* **2013**, *6*, 3380–3386.
- (20) Jeantelot, G.; Qureshi, M.; Harb, M.; Ould-Chikh, S.; Anjum, D. H.; Abou-Hamad, E.; Aguilar-Tapia, A.; Hazemann, J.-L.; Takanabe, K.; Basset, J.-M. TiO₂-Supported Pt Single Atoms by Surface Organometallic Chemistry for Photocatalytic Hydrogen Evolution. *Phys. Chem. Chem. Phys.* **2019**, *21*, 24429–24440.
- (21) Liu, J.; Xu, S.-M.; Li, Y.; Zhang, R.; Shao, M. Facet Engineering of WO₃ Arrays toward Highly Efficient and Stable Photoelectrochemical Hydrogen Generation from Natural Seawater. *Appl. Catal., B* **2020**, *264*, No. 118540.
- (22) Sivula, K.; Le Formal, F.; Grätzel, M. Solar Water Splitting: Progress Using Hematite (α -Fe₂O₃) Photoelectrodes. *ChemSusChem* **2011**, *4*, 432–449.
- (23) Higashi, M.; Domen, K.; Abe, R. Highly Stable Water Splitting on Oxynitride TaON Photoanode System Under Visible Light Irradiation. *J. Am. Chem. Soc.* **2012**, *134*, 6968–6971.
- (24) Solarska, R.; Jurczakowski, R.; Augustynski, J. A Highly Stable, Efficient Visible-Light Driven Water Photoelectrolysis System Using a Nanocrystalline WO₃ Photoanode and a Methane Sulfonic acid Electrolyte. *Nanoscale* **2012**, *4*, 1553–1556.
- (25) Li, Y.; Zhang, L.; Torres-Pardo, A.; González-Calbet, J. M.; Ma, Y.; Oleynikov, P.; Terasaki, O.; Asahina, S.; Shima, M.; Cha, D.; et al. Cobalt Phosphate-Modified Barium-Doped Tantalum Nitride Nanorod Photoanode with 1.5% Solar Energy Conversion Efficiency. *Nat. Commun.* **2013**, *4*, No. 2566.
- (26) Liu, G.; Shi, J.; Zhang, F.; Chen, Z.; Han, J.; Ding, C.; Chen, S.; Wang, Z.; Han, H.; Li, C. A Tantalum Nitride Photoanode Modified with a Hole-storage Layer for Highly Stable Solar water Splitting. *Angew. Chem., Int. Ed.* **2014**, *53*, 7295–7299.
- (27) Kim, T. W.; Choi, K.-S. Nanoporous BiVO₄ Photoanodes with Dual-Layer Oxygen Evolution Catalysts for Solar Water Splitting. *Science* **2014**, *343*, 990–994.
- (28) Cho, I.-S.; Kwak, C. H.; Kim, D. W.; Lee, S.; Hong, K. S. Photophysical, Photoelectrochemical, and Photocatalytic Properties of Novel Semiconductors with Narrow Band Gaps. *J. Phys. Chem. C* **2009**, *113*, 10647–10653.
- (29) Ziani, A.; Harb, M.; Noureldine, D.; Takanabe, K. UV-Visible Optoelectronic Properties of α -SnWO₄: A Comparative Experimental and Density Functional Theory Based Study. *Appl. Phys. Lett.* **2015**, *3*, No. 096101.
- (30) Pyper, K. J.; Evans, T. C.; Bartlett, B. M. Synthesis of α -SnWO₄ Thin-Film Electrodes by Hydrothermal Conversion from Crystalline WO₃. *Chin. Chem. Lett.* **2015**, *26*, 474–478.
- (31) Zhu, Z.; Sarker, P.; Zhao, C.; Zhou, L.; Grimm, R. L.; Huda, M. N.; Rao, P. M. Photoelectrochemical Properties and Behavior of α -SnWO₄ Photoanodes Synthesized by Hydrothermal Conversion of WO₃ Films. *ACS Appl. Mater. Interfaces* **2017**, *9*, 1459–1470.
- (32) Kölbach, M.; Pereiro, I. J.; Harbauer, K.; Plate, P.; Höflich, K.; Berglund, S. P.; Friedrich, D.; van der Krol, R.; Abdi, F. F. Revealing the Performance-Limiting Factors in α -SnWO₄ Photoanodes for Solar Water Splitting. *Chem. Mater.* **2018**, *30*, 8322–8331.
- (33) Zhang, X.; You, X.; Wang, X.; Yu, C.; Xu, L.; Wang, C.; Song, Y.; Zhang, F. Nest-Like α -SnWO₄ Nanostructures Assembled by Nanowires: Facile Synthesis and their Superior Photocatalytic Performance. *J. Alloys Compd.* **2019**, *802*, 502–510.
- (34) Kölbach, M.; Hempel, H.; Harbauer, K.; Schleuning, M.; Petsiuk, A.; Höflich, K.; Deinhart, V.; Friedrich, D.; Eichberger, R.; Abdi, F. F.; et al. Grain Boundaries Limit the Charge Carrier Transport in Pulsed Laser Deposited α -SnWO₄ Thin Film Photoabsorbers. *ACS Appl. Energy Mater.* **2020**, *3*, 4320–4330.
- (35) Kuzmin, A.; Anspoks, A.; Kalinko, A.; Timoshenko, J.; Kalendarev, R. External Pressure and Composition Effects on the Atomic and Electronic Structure of SnWO₄. *Sol. Energy Mater. Sol. Cells* **2015**, *143*, 627–634.
- (36) Huang, B.; Hart, J. N. DFT Study of Various Tungstates for Photocatalytic Water Splitting. *Phys. Chem. Chem. Phys.* **2020**, *22*, 1727–1737.
- (37) Harb, M.; Sautet, P.; Nurlaela, E.; Raybaud, P.; Cavallo, L.; Domen, K.; Basset, J.-M.; Takanabe, K. Tuning the Properties of Visible-Light-Responsive Tantalum (Oxy)Nitride Photocatalysts by Non-Stoichiometric Compositions: A First-Principles Viewpoint. *Phys. Chem. Chem. Phys.* **2014**, *16*, 20548–20560.
- (38) Noureldine, D.; Lardhi, S.; Ziani, A.; Harb, M.; Cavallo, L.; Takanabe, K. Combined Experimental-Theoretical Study of the Optoelectronic Properties of Non-Stoichiometric Pyrochlore Bismuth Titanate. *J. Mater. Chem. C* **2015**, *3*, 12032–12039.
- (39) Lardhi, S.; Noureldine, D.; Harb, M.; Ziani, A.; Cavallo, L.; Takanabe, K. Determination of the Electronic, Dielectric, and Optical Properties of Sillénite Bi₁₂TiO₂₀ and Perovskite-Like Bi₄Ti₃O₁₂ Materials from Hybrid First-Principle Calculations. *J. Chem. Phys.* **2016**, *144*, No. 134702.
- (40) Jang, J.-W.; Friedrich, D.; Müller, S.; Lamers, M.; Hempel, H.; Lardhi, S.; Cao, Z.; Harb, M.; Cavallo, L.; Heller, R.; et al. Enhancing Charge Carrier Lifetime in Metal Oxide Photoelectrodes through Mild Hydrogen Treatment. *Adv. Energy Mater.* **2017**, *7*, No. 1701536.

- (41) Lardhi, S.; Curutchet, A.; Cavallo, L.; Harb, M.; Le Bahers, T. Ab Initio Assessment of $\text{Bi}_{1-x}\text{RE}_x\text{CuOS}$ (RE = La, Gd, Y, Lu) Solid Solutions as a Semiconductor for Photochemical Water Splitting. *Phys. Chem. Chem. Phys.* **2017**, *19*, 12321–12330.
- (42) Lardhi, S.; Cavallo, L.; Harb, M. Determination of the Intrinsic Defect at the Origin of the Poor H_2 Evolution Performance of the Monoclinic BiVO_4 Photocatalyst Using Density Functional Theory. *J. Phys. Chem. C* **2018**, *122*, 18204–18211.
- (43) Heyd, J.; Scuseria, G. E.; Ernzerhof, M. Hybrid Functionals Based on a Screened Coulomb Potential. *J. Chem. Phys.* **2003**, *118*, 8207–8215.
- (44) Heyd, J.; Scuseria, G. E.; Ernzerhof, M. Erratum: “Hybrid Functionals Based on a Screened Coulomb Potential” [*J. Chem. Phys.* **118**, 8207 (2003)]. *J. Chem. Phys.* **2006**, *124*, No. 219906.
- (45) Harb, M.; Jeantelot, G.; Basset, J.-M. Insights into the Most Suitable TiO_2 Surfaces for Photocatalytic O_2 and H_2 Evolution Reactions from DFT Calculations. *J. Phys. Chem. C* **2019**, *123*, 28210–28218.
- (46) Harb, M.; Basset, J.-M. Predicting the Most Suitable Surface Candidates of Ta_3N_5 Photocatalysts for Water-Splitting Reactions Using Screened Coulomb Hybrid DFT Computations. *J. Phys. Chem. C* **2020**, *124*, 2472–2480.
- (47) Lardhi, S.; Cavallo, L.; Harb, M. Significant Impact of Exposed Facets on the BiVO_4 Material Performance for Photocatalytic Water Splitting Reactions. *J. Phys. Chem. Lett.* **2020**, *11*, 5497–5503.
- (48) Van de Walle, C. G.; Martin, R. M. Theoretical Study of Band Offsets at Semiconductor Interfaces. *Phys. Rev. B* **1987**, *35*, 8154–8165.
- (49) Franciosi, A.; Van de Walle, C. G. Heterojunction Band Offset Engineering. *Surf. Sci. Rep.* **1996**, *25*, 1–140.
- (50) Rossmesl, J.; Skúlason, E.; Björketun, M. E.; Tripkovic, V.; Nørskov, J. K. Modeling the Electrified Solid-Liquid Interface. *Chem. Phys. Lett.* **2008**, *466*, 68–71.
- (51) Stevanović, V.; Lany, S.; Ginley, D. S.; Tumasb, W.; Zunger, A. Assessing Capability of Semiconductors to Split water Using Ionization Potentials and Electron Affinities Only. *Phys. Chem. Chem. Phys.* **2014**, *16*, 3706–3714.
- (52) Pham, T. A.; Ping, Y.; Galli, G. Modelling Heterogeneous Interfaces for Solar Water Splitting. *Nat. Mater.* **2017**, *16*, 401–408.
- (53) Man, I. C.; Su, H.-Y.; Calle-Vallejo, F.; Hansen, H. A.; Martínez, J. I.; Inoglu, N. G.; Kitchin, J.; Jaramillo, T. F.; Nørskov, J. K.; Rossmesl, J. Universality in Oxygen Evolution Electrocatalysis on Oxide Surfaces. *ChemCatChem* **2011**, *3*, 1159–1165.
- (54) Kresse, G.; Hafner, J. Ab Initio Molecular-Dynamics Simulation of the Liquid-Metal-Amorphous-Semiconductor Transition in Germanium. *Phys. Rev. B* **1994**, *49*, 14251–14269.
- (55) Kresse, G.; Furthmüller, J. Efficient Iterative Schemes for Ab-Initio Total-Energy Calculations Using a Plane-Wave Basis Set. *Phys. Rev. B* **1996**, *54*, 11169–11186.
- (56) Kresse, G.; Furthmüller, J. Efficiency of Ab-Initio Total Energy Calculations for Metals and Semiconductors Using a Plane-Wave Basis Set. *Comput. Mater. Sci.* **1996**, *6*, 15–50.
- (57) Kresse, G.; Joubert, D. From Ultrasoft Pseudopotentials to the Projector Augmented-Wave Method. *Phys. Rev. B* **1999**, *59*, 1758–1775.
- (58) Perdew, J. P.; Burke, K.; Ernzerhof, M. Generalized Gradient Approximation Made Simple. *Phys. Rev. Lett.* **1996**, *77*, 3865–3868.
- (59) Blöchl, P. E. Projector Augmented-Wave Method. *Phys. Rev. B* **1994**, *50*, 17953–17979.
- (60) Monkhorst, H. J.; Pack, J. D. Special Points for Brillouin-Zone Integration. *Phys. Rev. B* **1976**, *13*, 5188–5192.
- (61) Makov, G.; Payne, M. C. Periodic Boundary Conditions in Ab Initio Calculations. *Phys. Rev. B* **1995**, *51*, 4014–4022.
- (62) Grimme, S.; Antony, J.; Ehrlich, S.; Krieg, H. A Consistent and Accurate Ab Initio Parametrization of Density Functional Dispersion Correction (DFT-D) for the 94 Elements H-Pu. *J. Chem. Phys.* **2010**, *132*, No. 154104.
- (63) Grimme, S.; Ehrlich, S.; Goerigk, L. Effect of the Damping Function in Dispersion Corrected Density Functional Theory. *J. Comput. Chem.* **2011**, *32*, 1456–1465.
- (64) Harb, M.; Cavallo, L.; Basset, J.-M. Remarkable Influence of $\alpha\text{-SnWO}_4$ Exposed facets on Their Photocatalytic Performance for H_2 and O_2 Evolution Reactions. *J. Phys. Chem. C* **2020**, *124*, 18684–18689.